Progress In Electromagnetics Research M, Vol. 125, 51-61, 2024

PIER M

(Received 26 January 2024, Accepted 29 February 2024, Scheduled 12 March 2024)

An Adaptive Mesh Global Modeling Method for Solving Non-Ideal Sliding Electrical Contact Problems

Jian Sun[1,2], Junsheng Cheng[1,2,3,*], Ling Xiong[2], Yuantao Cong[1,2], and Heyang Wang[1,2]

[1] *University of Chinese Academy of Sciences, Beijing 100049, China*
[2] *Institute of Electrical Engineering, Chinese Academy of Sciences, Beijing 100190, China*
[3] *Institute of Electrical Engineering and Advanced Electromagnetic Drive Technology, Qilu Zhongke, Jinan, China*

ABSTRACT: The armature and rail sizes of electromagnetic rail launcher vary greatly, and the refined 3D finite element computation occupies a large amount of physical memory. In order to enhance the economy of dynamic computation, this paper proposes an adaptive hexahedral mesh method based on mesh expansion, compression, and translation. In addition, split nodes are used on both sides of the contact surface, and interface conditions and frictional heat sources are constrained through point penalty function method to solve non-ideal sliding electrical contact problems. Comparative calculations with the same type of software and the same model are carried out, and the results calculated in this paper are consistent with the relevant results of MEAP3D. This paper also compares the EMRL calculation results of adaptive mesh model and constant mesh model to verify the reliability of the method. In addition, the C-type EMRLs are compared and analyzed. The results show that due to the influence of velocity skin effect, the dynamic inductance gradient of the rail gradually increases over time and is greater than the static value. The maximum difference between the two is 5.65% of the dynamic inductance gradient. The steel shell generates eddy currents, causing a decrease in armature velocity of 4.7 m/s under the small caliber launcher. The maximum eddy current density waveform of the shell exhibits two peaks. In the frictionless heat, the temperature of the armature is underestimated, and under the action of frictional heat, the trailing edge of the armature is ablated and melted.

1. INTRODUCTION

Electromagnetic rail launcher (EMRL) is a device that utilizes electromagnetic energy to accelerate a load to a high speed. Its operation is characterized by the presence of large currents between high-speed sliding electrical contacts, also known as the sliding electrical contact phenomenon. The device typically utilizes pulsed capacitor discharges for electrical energy input. The combination of pulsed high-current feed and the velocity skin effect (VSE) at high-speed motion can result in current densities in the conductor that are on the order of GA/m^2 [1–3]. This in turn produces localized high heat accumulation, forming metal interface damage [4–6] and affecting service life [7, 8]. Understanding the spatio-temporal evolution of multi-physics parameters in EMRL can help to improve the overall performance. Unfortunately, for current laboratory environments, diagnostic and measurement methods available for physical quantities in the chamber are very limited [9–11], so it is satisfactory to model the operational processes of the device with the help of advanced modeling and simulation tools. However, unlike non-contact dynamic electromagnetic field solutions such as linear and rotating motors, the stator and rotor in EMRL are in direct electrical contact, and there is no air gap between them. Therefore, it is difficult for existing commercial software to simulate the operation process of EMRL.

Although analytical and traditional difference methods have many limitations when facing complex multiphysics problems, they provide some initial understanding of the field distribution of EMRL. Based on the Biot-Savat law and considering the skin effect of current distribution, Nie et al. derived the spatial magnetic field distribution of rectangular aperture [12]. Through parametric simulations, Keshtakar calculated the current density and magnetic flux density distribution of two-dimensional rail sections of different sizes [13]. To predict transition in railguns, Gong and Weng developed a three-dimensional numerical model of current melt-wave erosion (MWE) and used the Douglas-Brian finite difference method to simulate the formation and propagation of MWE [14].

The widespread application of finite element method in the field of electromagnetic launch has greatly promoted people's understanding of EMRL multi-field coupling. Shvetsov and Stankevich used the stationary solutions of the Maxwell equations to calculate the current distribution of EMRL [15, 16]. Using the Lagrange formula, Hsieh established mechanical, electromagnetic, and thermal coupling algorithms, and it has been widely used [17, 18]. Lin and Li developed a field circuit coupling algorithm to model the circuit behavior and electromagnetic field details of electromagnetic railguns [19], and then some actual factors, such as material nonlinearity, structural deformation, contact and collision, are also accounted in the model [20]. Wang et al. discretized the control equations of the electric field E and magnetic field B in an electric conductor to obtain a local refined solution for railgun [21].

Although numerical simulation technology in EMRL continues to advance with the deepening of research, the current

* Corresponding author: Junsheng Cheng (jscheng@mail.iee.ac.cn).

computer technology still faces challenges in simulating full-scale launchers. Armature sizes of several centimeters need to be finely dissected, and rail can be several meters long, so the contradiction between large-scale calculations and fine-grained solutions persists. And non-ideal electrical contact conditions such as frictional heat should be fully considered.

In this paper, frictional heat is applied on both sides of the armature and rail by splitting the nodes and heat distribution coefficients, aiming to seek solutions for non-ideal electrical contact interfaces. The dynamic launch process of MERL is solved by an adaptive mesh method with extended, compressed, and translating meshes. A small number of meshes are available to complete the 3D numerical simulation, which greatly saves memory and does not require changing the element and node information during the computation. The reliability of the model is verified by comparing it with the same model in EMAP3D, as well as comparing the constant mesh model and the adaptive mesh model under the same excitation conditions. In addition, the velocity skin effect, steel shell eddy current, and friction heat source of C-type armature are compared and analyzed.

2. MATHEMATICAL PHYSICAL MODEL OF THE SLIDING ELECTRICAL CONTACT PROBLEM

2.1. Basic Theory of Electromagnetic and Thermal Fields

A simplified EMRL diagram of the dynamic process is shown in Fig. 1, and only a 1/4 model is built considering the symmetry of the model. The current flows in from the breech face of the rail and flows out through the midplane of the armature. The armature moves forward under electromagnetic thrust. The electromagnetic field control equations of EMRL can be described using vector magnetic potential $\mathbf{A}$ and scalar potential φ as basic quantities. The Galerkin format of the electromagnetic field equations is obtained.

$$\int_V \left(\mathbf{W}_j \cdot \nabla \times \frac{1}{\mu} \nabla \times \mathbf{A} + \sigma \mathbf{W}_j \cdot \nabla \varphi + \sigma \mathbf{W}_j \cdot \frac{d\mathbf{A}}{dt}\right) dV = 0 \quad (1)$$

$$\int_V W_j \, \nabla \cdot \left(-\sigma \nabla \varphi - \sigma \frac{d\mathbf{A}}{dt}\right) dV = 0 \quad (2)$$

where μ is the magnetic permeability, σ the electrical conductivity, t the time, $\mathbf{W}$ the vector weight function, and W the scalar weight function. Use 8-node hexahedral elements to mesh the solution domain, then

$$\begin{aligned} W &= \left[\begin{array}{cccccccc} W_1 & W_2 & W_3 & W_4 & W_5 & W_6 & W_7 & W_8 \end{array}\right] \\ W_j &= \frac{(1+\xi\xi_j)(1+\eta\eta_j)(1+\zeta\zeta_j)}{8}, \quad (j = 1, 2, \ldots, 8) \end{aligned} \quad (3)$$

Since Eqs. (1) and (2) involve the derivative terms of shape functions for global coordinates as well as local coordinates, Jacobian matrix is used to perform this transformation.

$$J_a = \left[\begin{array}{ccc} \frac{\partial x}{\partial \xi} & \frac{\partial y}{\partial \xi} & \frac{\partial z}{\partial \xi} \\ \frac{\partial x}{\partial \eta} & \frac{\partial y}{\partial \eta} & \frac{\partial z}{\partial \eta} \\ \frac{\partial x}{\partial \zeta} & \frac{\partial y}{\partial \zeta} & \frac{\partial z}{\partial \zeta} \end{array}\right] = \left[\begin{array}{ccc} \sum_{i=1}^{8} \frac{\partial W_i}{\partial \xi} x_i & \sum_{i=1}^{8} \frac{\partial W_i}{\partial \xi} y_i & \sum_{i=1}^{8} \frac{\partial W_i}{\partial \xi} z_i \\ \sum_{i=1}^{8} \frac{\partial W_i}{\partial \eta} x_i & \sum_{i=1}^{8} \frac{\partial W_i}{\partial \eta} y_i & \sum_{i=1}^{8} \frac{\partial W_i}{\partial \eta} z_i \\ \sum_{i=1}^{8} \frac{\partial W_i}{\partial \zeta} x_i & \sum_{i=1}^{8} \frac{\partial W_i}{\partial \zeta} y_i & \sum_{i=1}^{8} \frac{\partial W_i}{\partial \zeta} z_i \end{array}\right] \quad (4)$$

The backward Euler method is used for numerical discretization.

$$\left[\mathbf{C} + \frac{\mathbf{M}}{\Delta \mathbf{t}}\right] \left[\mathbf{A}_\varphi^{\mathbf{t}+\Delta\mathbf{t}}\right] = \left[\frac{\mathbf{M}}{\Delta \mathbf{t}}\right] \left[\mathbf{A}_\varphi^{\mathbf{t}}\right] \quad (5)$$

where $\mathbf{C}$ is the stiffness matrix; $\mathbf{M}$ is the damping matrix; and $\mathbf{A}_\varphi^{t+\Delta t}$ are the unknown quantities at the current time and $\mathbf{A}_\varphi^{t}$ the previous time respectively.

The initial value of Eq. (5) is zero, i.e., $\mathbf{A}_\varphi^0 = 0$. In addition, boundary conditions need to be specified.

For the front surface and left surface of the solution domain, the normal component of the magnetic field is zero. In addition, the tangential components of the current are also zero for the inflow and outflow end faces of the current in the conductors. This process is described as follows:

$$\mathbf{n} \times \mathbf{A} = \mathbf{0} \quad (6)$$

$$\varphi = \text{constant} \quad (7)$$

On the midplane of the armature, the electric scalar φ can be set to zero as a reference. For the bottom surface of the solution domain, the tangential component of the magnetic field is zero.

$$\mathbf{n} \cdot \mathbf{A} = \mathbf{0} \quad (8)$$

The tangential component of the vector magnetic potential can be specified as zero for the remaining surfaces in the solution domain.

$\mathbf{A}$ and φ can be converted into $\mathbf{B}$ and $\mathbf{J}$. Finally, the electromagnetic thrust, velocity, and displacement of the armature are obtained.

The Joule heat calculated by the electromagnetic field is used as the internal heat source, and the thermal field equation is obtained by the discretization of finite elements.

$$\int_V \lambda \nabla W_j \cdot \nabla T dV + \int_V \rho c \frac{\partial T}{\partial t} W_j dV = \int_V \frac{J^2}{\sigma} W_j dV \quad (9)$$

where T is the temperature, ρ the mass density, c the specific heat, and λ the thermal conductivity.

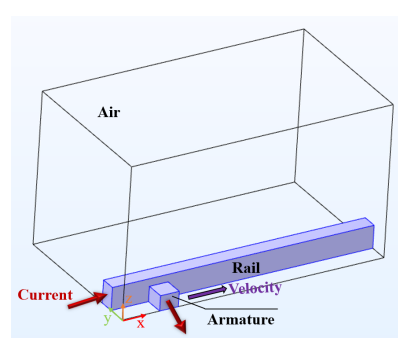

FIGURE 1. Simplified schematic of a typical 1/4 EMRL model.

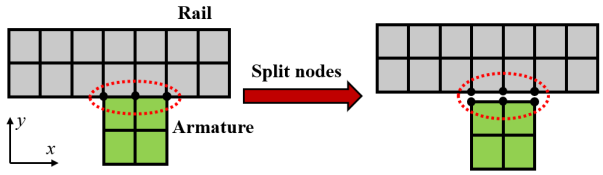

FIGURE 2. Schematic of contact interface splitting nodes.

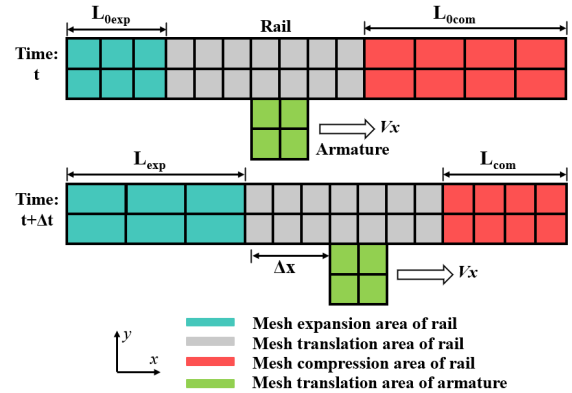

FIGURE 3. Schematic of adaptive mesh time evolution for moving conductors.

The frictional heat during the launch process is applied in the form of a surface heat source.

$$S_f = \mu_c P_c v \tag{10}$$

where μ_c is the coefficient of friction, and P_c is the contact pressure.

On both sides of the contact surface, frictional heat sources need to be applied separately. The frictional heat sources on the armature side and rail side are determined by their respective heat partitioning coefficients. The subscript 'a' represents the armature, and 'r' represents the rail.

$$\eta_a = \frac{\sqrt{\lambda_a \rho_a c_a}}{\sqrt{\lambda_a \rho_a c_a} + \sqrt{\lambda_r \rho_r c_r}} \tag{11}$$

$$\eta_r = \frac{\sqrt{\lambda_r \rho_r c_r}}{\sqrt{\lambda_a \rho_a c_a} + \sqrt{\lambda_r \rho_r c_r}} \tag{12}$$

The matrix format for the thermal field equation is:

$$\left[\mathbf{C}_T + \frac{\mathbf{M}_T}{\Delta \mathbf{t}}\right]\left[\mathbf{T}^{\mathbf{t}+\Delta t}\right] = \left[\frac{\mathbf{M}_T}{\Delta \mathbf{t}}\right]\left[\mathbf{T}^{\mathbf{t}}\right] \tag{13}$$

where $\mathbf{C}_T$ is the stiffness matrix of thermal field, and $\mathbf{M}_T$ is the damping matrix of thermal field.

The initial temperature in the solution domain is 300 K. Compared to Joule heating, the heat transfer between the conductor and air is negligible.

2.2. Interface Processing Based on Split Nodes

Different from motors and magnetic levitation devices, the armature acceleration process of EMRL is a typical sliding electrical contact process. The armature is in direct contact with the rail, so the boundary conditions need special consideration at the contact interface between them.

In this paper, each side of the contact interface is subordinate to a set of nodes as shown in Fig. 2. The nodes corresponding to the armature and the rail satisfy the conditions of vector magnetic potential continuity as well as scalar potential discontinuity [22].

$$\mathbf{A}_r = \mathbf{A}_a \tag{14}$$

$$\varphi_a - \varphi_r = -\mathbf{v} \cdot \mathbf{A}_r \tag{15}$$

Equations (14) and (15) indicate that $\mathbf{A}$ is continuous on both sides of the interface, while φ is discontinuous. This constraint ensures the continuity of the tangential component of the electric field, and the continuity of the normal and tangential directions of the magnetic field. To illustrate the application of interface constraints, Eq. (5) is redefined as:

$$[\mathbf{K}]\left[\mathbf{A}_{\varphi}^{\mathbf{t}+\Delta\mathbf{t}}\right] = [\mathbf{F}] \tag{16}$$

where $\mathbf{K}$ is the coefficient matrix, and $\mathbf{F}$ is the right term of the equation.

In this paper, the method of point penalty function is used to impose constraint equations.

$$\begin{aligned} \mathbf{K}' &= \mathbf{K} + \sum_{i=1}^{N} \alpha Q_i Q_i^T + \sum_{i=1}^{N} \beta Q_i Q_i^T \\ \mathbf{F}' &= \mathbf{F} + \sum_{i=1}^{N} \beta f_i Q_i \\ f_i &= -v_x \cdot A_{rxi} \end{aligned} \tag{17}$$

where $\mathbf{K}'$ is the total coefficient matrix, $\mathbf{F}'$ the total right term of the equation, N the number of one-sided nodes on the interface, Q the point penalty function matrix, f the difference matrix of φ, and α and β are the penalty factors for Eqs. (14) and (15), respectively.

2.3. Adaptive Mesh Method for Moving Conductor

Due to the significant difference in scale between the armature and the rail, the traditional method of uniformly distributing the mesh along the acceleration direction of the armature will result in a huge data scale. This significantly increases the computational cost. In this paper, a flexible and economical adaptive mesh method is proposed to reduce the number of meshes and computational cost.

As shown in Fig. 3, at the initial moment, mesh refinement is only performed in the contact area. The meshes outside the contact area are adjusted appropriately as the armature moves.

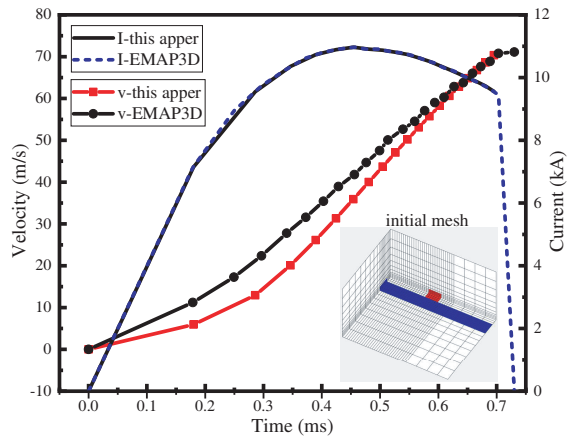

FIGURE 4. Comparison of current and velocity waveforms.

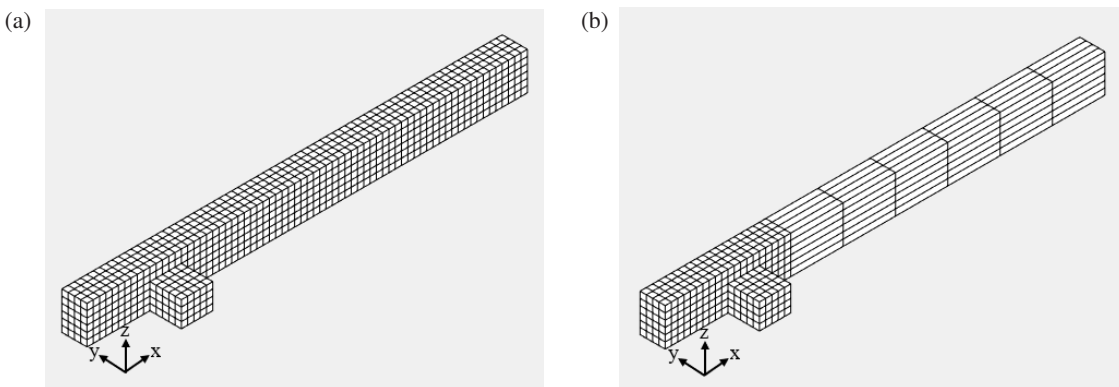

FIGURE 5. Schematic of initial conductor meshes (1/4 model). (a) Constant mesh. (b) Adaptive mesh.

The meshes behind the contact area expand as the armature moves forward, while the meshes in front of the contact area compress. In the traditional constant mesh method, since interlacing of meshes is not tolerated, the armature is forced to move one mesh length per time step. However, the adaptive mesh approach overcomes this limitation and is more flexible.

$$\begin{aligned} L_{\text{exp}} &= L_{0\,\text{exp}} + \Delta x \\ L_{com} &= L_{0com} - \Delta x \end{aligned} \tag{18}$$

where $L_{0\,\text{exp}}$ and L_{exp} are the initial and final lengths of the expanded area at each time step; L_{0com} and L_{com} are the initial and final lengths of the compressed area at each time step; and Δx is the displacement within Δt time.

The expansion and compression of the mesh will result in a larger mesh aspect ratio. But these changes in mesh shape do not have much effect on the accuracy of the calculation results. This is because the physical quantity only changes dramatically in the contact region, while the distal region has the property of shift invariant.

Furthermore, Eqs. (5) and (13) show that the calculation requires the physical values of the previous moment. However, the movement of the armature causes the mesh to change. Therefore, the physical values of the previous moment after the mesh change need to be interpolated to obtain.

3. RESULTS ANALYSIS OF CONSTANT MESH MODEL AND ADAPTIVE MESH MODEL

In order to verify the correctness of the established adaptive mesh method, the calculations are carried out using the same armature-rail model and input conditions as in the literature [17], and the results were compared with EMAP3D. The armature exit calculated in this paper is 70.35 m/s, while the corresponding value calculated by EMAP3D is 71.12 m/s, with a difference of 0.77 m/s. A comparison of the current waveforms of this paper and EMAP3D is shown in Fig. 4, in which the process of the armature gradually detaching from the rail is not calculated. The current curves of the two match very well.

In addition, the constant mesh calculation and adaptive mesh calculation with the same geometrical model and excitation conditions are performed and compared. The armature is a 5 mm × 5 mm × 4 mm block, and the rail is a 70 mm × 4 mm × 6 mm block. The armature material is 6061 aluminum alloy, and the rail material is brass. The material properties are shown in Table 1.

As shown in Fig. 5, for the constant mesh model, the conductor meshes are all cubes of length 1 mm. For the adaptive mesh model, the mesh in front of the contact area is relatively sparse at the initial moment (air mesh not shown). The armature midplane is the potential reference plane, and a constant

TABLE 1. Material parameters.

Parameters	Brass	6061 aluminum alloy
$\sigma_0/\mathrm{MS}\cdot\mathrm{m}^{-1}$, Initial electrical conductivity	14.08	25
$\mu/\mathrm{H}\cdot\mathrm{m}^{-1}$, Magnetic permeability	1.2566e-6	1.2566e-6
$\rho/\mathrm{kg}\cdot\mathrm{m}^{-3}$, Mass density	8500	2700
$c/\mathrm{J}\cdot(\mathrm{kg}\cdot\mathrm{K})^{-1}$, Specific heat	368	896
$\lambda/\mathrm{W}\cdot(\mathrm{m}\cdot\mathrm{K})^{-1}$, Thermal conductivity	109	167
α/K, Temperature coefficient of resistivity	0.002	0.0041
T_m/K, Melting temperature	1027	924.85

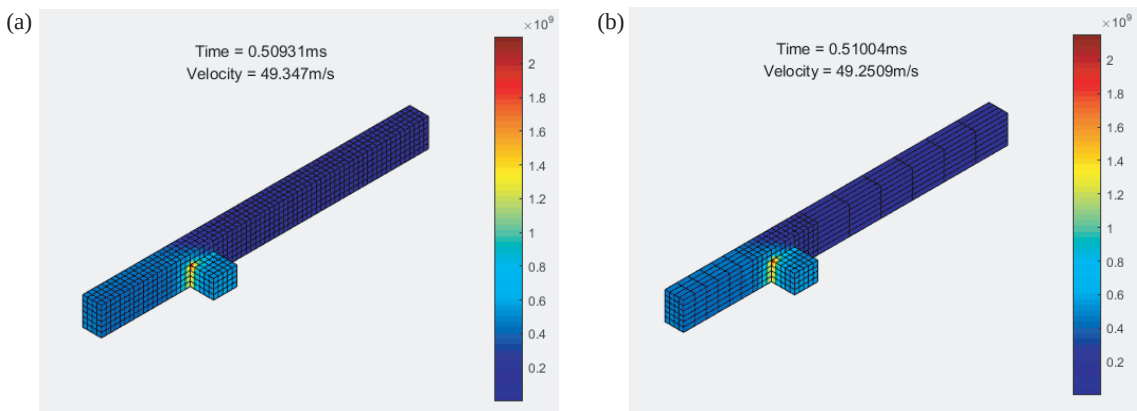

FIGURE 6. Three-dimensional current density distribution of rail and armature at about 0.5 ms ($\mathrm{A/m^2}$). (a) Constant mesh. (b) Adaptive mesh.

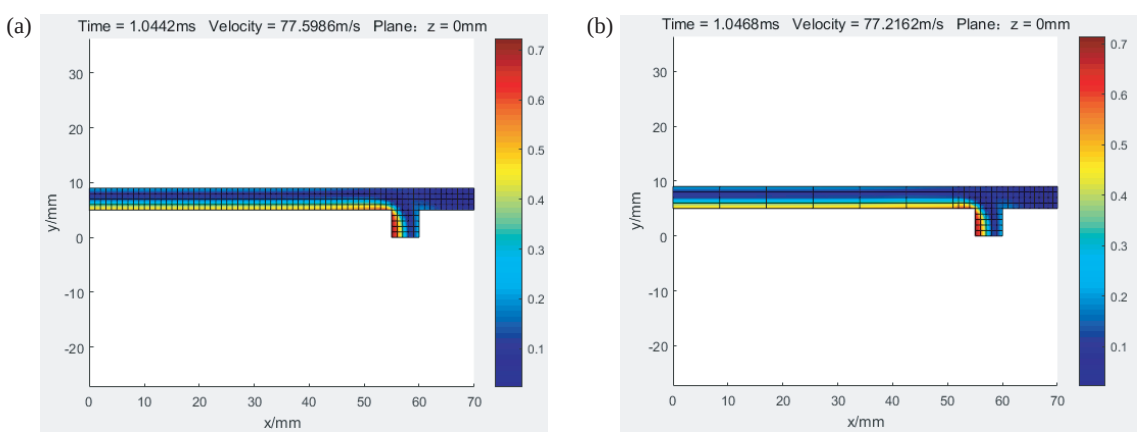

FIGURE 7. Two-dimensional magnetic induction intensity distribution of rail and armature at the exit time(T). (a) Constant mesh. (b) Adaptive mesh.

voltage of 0.9 volts is applied at the breech. Both calculations stop running when the armature moves a distance of 45 mm.

The finite element codes for constant mesh and adaptive mesh models are implemented by the Matlab platform (2020b) and the computer with the intel i9-10900 CPU @2.81 GHz and a 32 GB RAM. The parameter comparison between constant mesh and adaptive mesh is shown in Table 2. The number of elements as well as the number of nodes is greatly reduced in the adaptive mesh model. The number of electromagnetic field unknowns in the adaptive mesh model is 38.47% of that in the constant mesh model. This will greatly reduce the size of the matrix, thereby saving computational memory space. As the length of the rail in the calculation model increases, this advantage will become more apparent. It is worth noting that under the adaptive mesh method, the calculation time for each time step is about 159.83% of that of the constant mesh method. This is due to changes in mesh shape that require recalculation of the corresponding element stiffness matrix. This involves some symbolic operations, and Matlab has no obvious advantage in symbolic operations. Nevertheless, the adaptive mesh method provides the ability to perform large-scale model calculations with limited computer memory resources.

TABLE 2. Parameter comparison of constant mesh and adaptive mesh.

Parameters	Constant mesh	Adaptive mesh
Number of elements	9800	3640
Number of nodes	11745	4485
Number of unknowns (Electromagnetic field)	37900	14580
Calculation time(s) for one step (average)	580	927

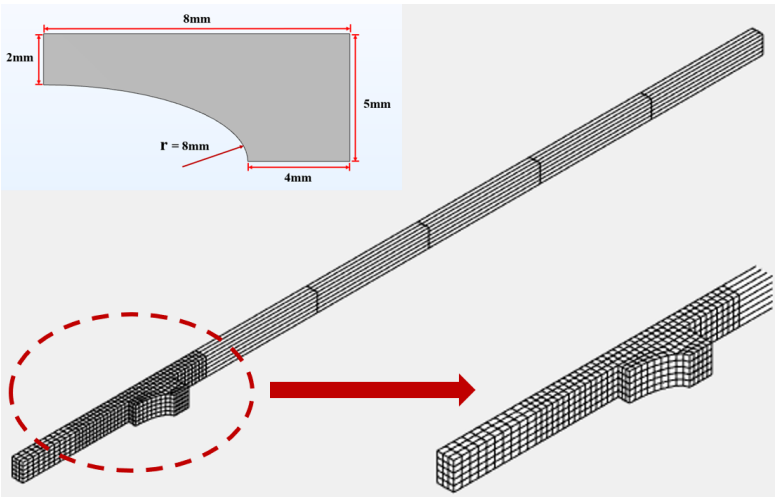

FIGURE 8. The initial mesh of the conductors and the geometry of the armature.

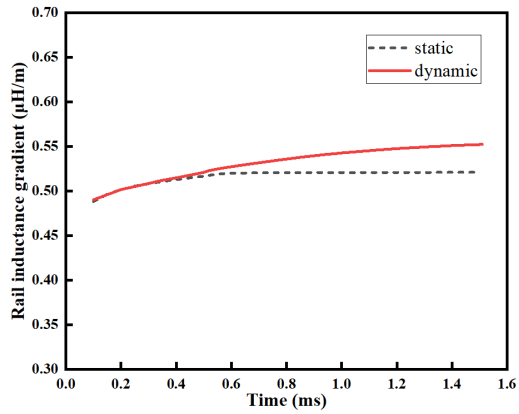

FIGURE 9. Rail inductance gradient waveforms under dynamic and static conditions.

Since the temperature field results are calculated from the electromagnetic field results, the electromagnetic physical quantities are the most direct comparison. For the sake of original comparison and analysis, the effect of friction on velocity was ignored for both calculations. Figs. 6 and 7 show the distributions of current density and magnetic induction for both cases. Mesh details are also shown. The physical quantities shrink significantly at the trailing edge of the contact under the velocity skin effect. These results fully justify the adaptive mesh method.

4. NUMERICAL ANALYSIS OF C-TYPE ARMATURE UNDER MULTI-FIELD COUPLING

The armature is often a C-type structure during the actual launch. In this section, the physical properties of the EMRL in the case of C-type armature are calculated and discussed using the material parameters in Table 1. The size of the copper alloy rail is 5 mm × 3 mm × 210 mm. The initial mesh of the conductors and the geometry of the armature are shown in Fig. 8.

The total dynamic calculation time is 1.51 ms; the time step is pre-specified; and the minimum time step is 15 μs. All velocity calculations in this section take into account friction and have a coefficient of friction of 0.1.

Pulse current is input into the conductor as an excitation. The current reaches 36 kA at 0.5 ms, and the current drops to 21.7 kA at the final time.

4.1. Analysis of Velocity Skin Effect

The rail inductance gradient (L') is an important parameter that characterizes the performance of the EMRL. For two-rail launcher, the rail inductance gradient is generally considered a constant of approximately 0.5 μH/m in order to quickly estimate electromagnetic thrust. In fact, during the launch process, the rail inductance gradient changes over time. According to magnetic field energy storage ($L' = \int_V BHdV/I^2x$), the transient inductance gradient can be obtained. Fig. 9 compares the inductance gradient under dynamic and static conditions. Under static conditions, the current of the rail diffuses uniformly after about 0.6 ms, so the rail inductance gradient tends to be stable. Under the influence of velocity skin effect (VSE), the dynamic inductance gradient obtained ranges from 0.4904 μH/m to 0.5524 μH/m. In the middle and late stages of launch, the dynamic inductance gradient is larger than the static corresponding value. The difference value is 5.65% of the dynamic inductance gradient at 1.5 ms.

Figure 10 shows the current density distributions under dynamic and static conditions at 0.6 ms. At this moment, the maximum current density of the rail under dynamic conditions is 2.1 times that of static conditions. One obvious feature is that under static conditions, the current distribution in the rail slightly behind the contact surface is relatively concentrated, but almost uniform along the height direction. Under dynamic conditions, the current distribution at this position is not uniform along the height direction and is concentrated at the top position.

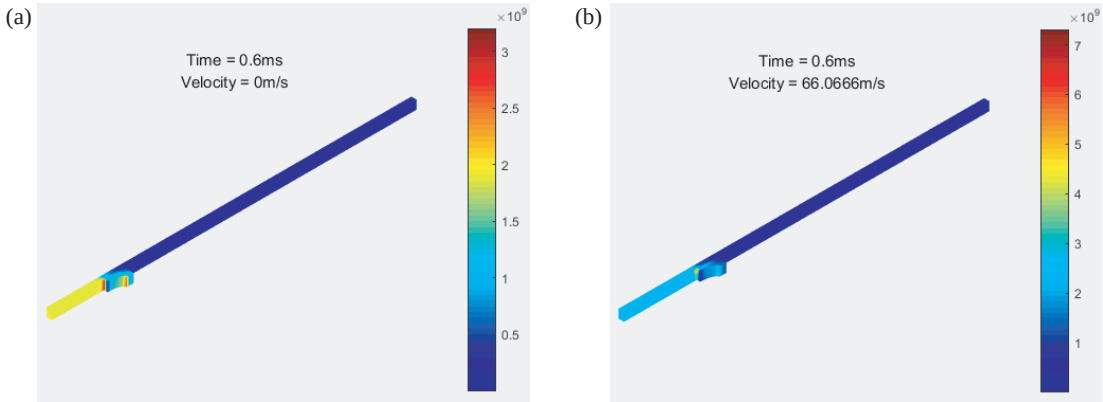

FIGURE 10. Current density distribution under static and dynamic conditions at 0.6 ms. (a) Static case. (b) Dynamic case.

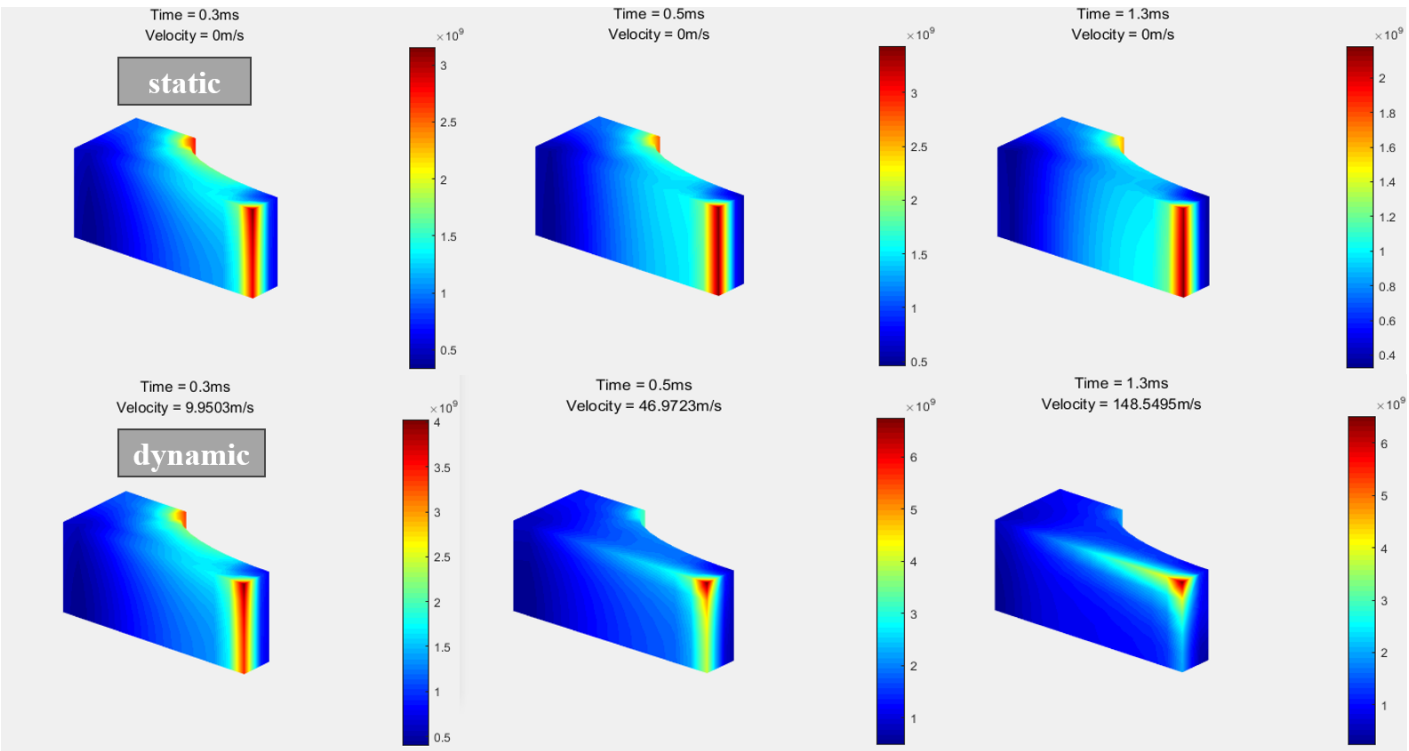

FIGURE 11. Evolution of armature current density distribution under static and dynamic conditions.

Due to the higher resistivity of brass compared to 6061 aluminum alloy, current is conducted along a low resistivity path under static conditions, and the current distribution at the tail of the armature is relatively concentrated. As time passes, the current on the contact surface spreads forward, as shown in the left column of Fig. 11. However, for the moving armature, the current gradually shrinks due to the influence of VSE, and the maximum current density value of the armature is greater than the value under static state at the same time. Moreover, there was no significant decrease in the maximum current density at the decreasing stage of the input current. In the later stage of the launch process, the current at the tailing edge of the armature shifts upwards, and the current at the outer edge extends forward.

As shown in Fig. 12(a), the static maximum temperature at 1.5 ms is 416.8 K, located in the rail slightly behind the contact position. For dynamic conditions, the maximum rail temperature is 429.6 K. And the maximum armature temperature can reach 819.3 K. This hot spot is located at the tail of the outer edge of the armature, which corresponds to the current distribution. In the initial stage, the velocity of the armature is relatively low, while the input current rapidly increases, resulting in a higher temperature in the rear of the rail, which is consistent with the experimental phenomenon.

In general, the velocity skin effect has a profound impact on the physical field distribution of the conductors, especially the outer edge of the armature and the tailing edge of the contact,

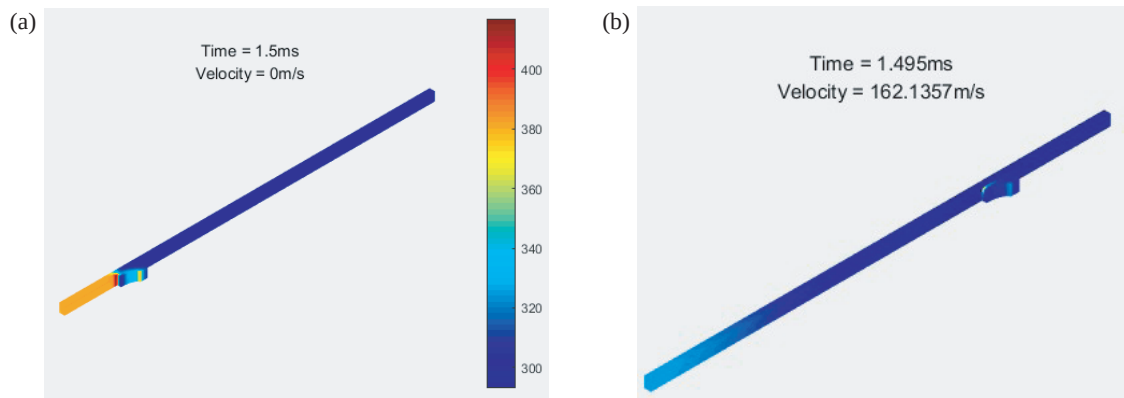

FIGURE 12. Temperature distribution under static and dynamic conditions at about 1.5 ms. (a) Static case. (b) Dynamic case.

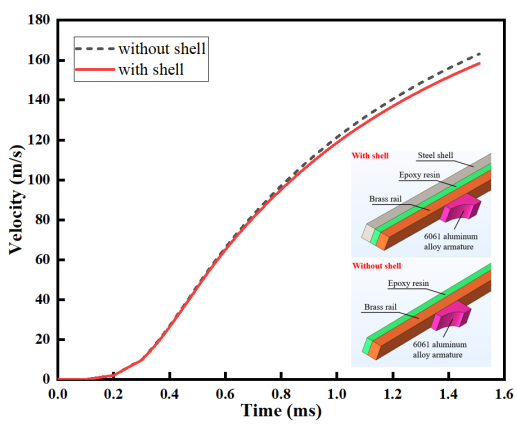

FIGURE 13. Comparison of velocities with and without shells.

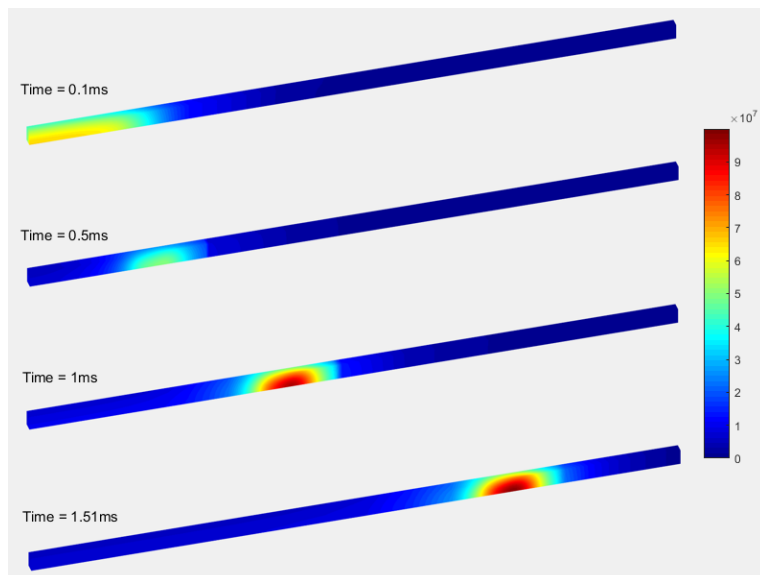

FIGURE 14. Evolution process of eddy current distribution in the steel shell (A/m^2).

because material softening and further damage are prone to occur here.

4.2. The Influence of Steel Shell on Velocity

During actual launch, the launchers require steel shells for encapsulation and preloading. Therefore, the 304 stainless steel shell with the same size as the rail is considered and calculated. The distance between the steel shell and steel rail is 2 mm. The epoxy resin is filled between the steel shell and the rail to maintain insulation.

Figure 13 shows the comparison of armature velocities with and without a shell. Under the same excitation, the velocity of the case with a steel shell is 4.7 m/s lower than that of the case without a steel shell. 304 stainless steel has a conductivity of 1.37 MS/m. Although this is an order of magnitude lower than the conductivity of 6061 aluminum armature and brass rail, eddy current losses are still generated, thus resulting in a decrease in the velocity of the armature.

The eddy current distribution evolution of the steel shell during the launch process is shown in Fig. 14. At 0.1 ms, the armature has not yet started to move, and only the skin effect of the pulse current exists. The eddy current of the steel shell is distributed in the breech and relatively uniform. As the armature moves, the steel shell eddy current is mainly located at the position of the armature. The eddy current concentration area presents a semielliptical shape, decaying from the bottom of the inner surface to the surrounding area.

The curve of the maximum eddy current density of the steel shell over time is shown in Fig. 15, which has two peaks. In fact, the eddy current in the steel shell consists of two parts, namely the motion induction term $\mathbf{J}_v$ ($\sigma v \times \nabla \times \mathbf{A}$) and the transient induction term $\mathbf{J}_t$ ($-\sigma \partial \mathbf{A}/\partial t$). In the initial stage, the transient induction term dominates, and as the armature velocity increases, the motion induction term begins to increase. It is believed that $\mathbf{J}_v$ and $\mathbf{J}_t$ have opposite effects in the rising stage of input current; therefore, the maximum eddy current density gradually decreases after the first peak in the initial stage. At

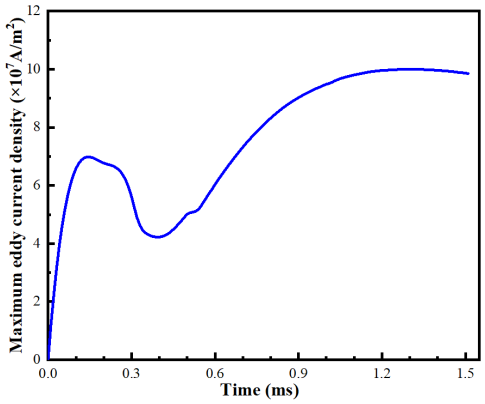

FIGURE 15. Maximum eddy current density waveform of steel shell.

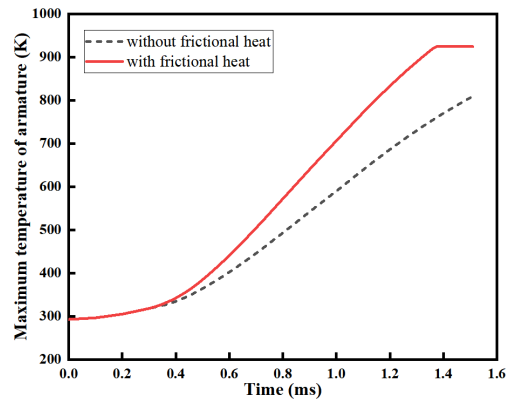

FIGURE 16. The maximum temperature waveform of the armature with and without frictional heat.

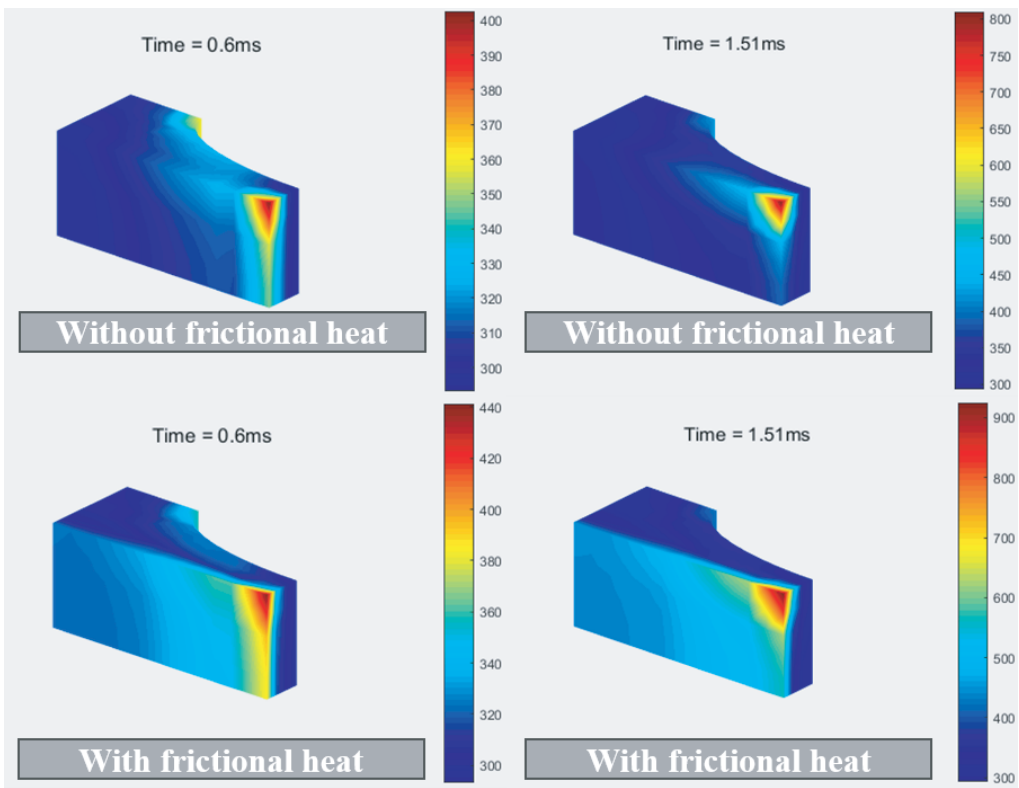

FIGURE 17. Armature temperature distribution under two cases of 0.6 ms and 1.51 ms.

0.5 ms, although the input current reaches its peak, the maximum eddy current density of the steel shell does not reach the peak, approximately 5.0102e+7 A/m^2. Then, the input current changes from the rising phase to the falling phase, and the transient induction term is reversed, and the motion induced term has also become larger, so the maximum eddy current density begins to increase. Finally, the curve of the maximum eddy current density of the steel shell has two peaks.

It is worth noting that the EMRL calculated in this paper belongs to the small caliber size, and under the large caliber, the eddy current loss of the steel shell is more significant, which will lead to a huge decrease in armature velocity. Accurately understanding the spatial and temporal distribution of the steel shell helps guide the launch process and further reduces its impact on system efficiency by optimizing the steel shell structure and materials.

4.3. The Influence of Frictional Heat on Armature Ablation

The 3D finite element calculation of the contact dynamic electromagnetic field problem is already quite difficult, so frictional heat is often ignored. In fact, frictional heat has a great influence on the armature ablation phenomenon during sliding electrical contact. Therefore, the two cases with and without

frictional heat source under the steel shell in this section are calculated and compared.

As shown in Fig. 16, after about 0.36 ms, the maximum temperature of the armature under the condition of frictional heat begins to be greater than that of frictionless heat. Then, the difference between the two gradually increased, reaching a maximum of 165.4 K. At 1.37 ms, considering the frictional heat, the armature reaches the melting temperature and begins to ablation. In the case of frictionless heat, there is no ablation of the armature during the entire calculation process. This shows the importance of frictional heat for the calculation results. Fig. 17 shows the details of the armature temperature distribution in two cases. With frictional heat, the armature tailing edge is first ablated and melted, and the high temperature area gradually expands forward along the contact surface.

5. CONCLUSION

In this paper, a multi-field coupled model of EMRL is developed based on the finite element method with adaptive hexahedral mesh. The same-condition comparison between the block armature model and EMAP3D is carried out, and the results are in good agreement. Under the same input conditions, the calculation results of the constant mesh and adaptive mesh models are consistent, which verifies the reliability of the model. The main conclusions are as follows:

a) The adaptive mesh approach allows for a significant reduction in physical memory while maintaining the accuracy of the computational results. It also eliminates the limitation that meshes cannot be interleaved, thus enabling more flexible and economical computations.

b) Under static conditions, the rail current tends to become uniform after about 0.6 ms, leading to a gradual stabilization of the rail static inductance gradient. Affected by the VSE, the rail dynamic inductance gradient gradually increases with time and is greater than the static value. The difference value is 5.65% of the dynamic inductance gradient at 1.5 ms.

c) The steel shell induces eddy currents, causing a decrease in armature velocity of 4.7 m/s. The eddy current concentration area presents a semielliptical shape, decaying from the bottom of the inner surface to the surrounding area. The superposition of the transient induction term and motion induction term of the eddy current during the launch process results in two peaks in the maximum eddy current density waveform.

d) Under the action of frictional heat, the trailing edge of the armature is first ablated and melted, and the high temperature region gradually extends along the contact surface in the sliding direction. In the absence of frictional heat, the armature temperature is underestimated, and the final armature temperature has not reached its melting point.

ACKNOWLEDGMENT

This work was supported in part by the CAS "Light of West China" Program under Grant xbzg-zdsys-202317, and in part by the Scientific Instrument Developing Project of the Chinese Academy of Sciences under Grant YJKYYQ20200011, and in part by the Joint fund of Chinese Academy of Sciences under Grant 8091A02, and in part by Institute of Electrical Engineering and the Advanced Electromagnetic Drive Technology, Qilu Zhongke Research Fund Project.

CONFLICT OF INTEREST

The authors declare that they have no known competing financial interests or personal relationships that could have appeared to influence the work reported in this paper.

REFERENCES

[1] Keshtkar, A., L. Gharib, M. S. Bayati, and M. Abbasi, "Simulation of a two-turn railgun and comparison between a conventional railgun and a two-turn railgun by 3-D FEM," *IEEE Transactions on Plasma Science*, Vol. 41, No. 5, 1392–1397, 2013.

[2] Xing, Y.-C., Q.-A. Lv, B. Lei, H.-J. Xiang, R.-G. Zhu, and C. Liu, "Analysis of transient current distribution in copper strips of different structures for electromagnetic railgun," *IEEE Transactions on Plasma Science*, Vol. 43, No. 5, 1566–1571, 2015.

[3] Li, C., L. Chen, Z. Wang, J. Ruan, P. Wu, J. He, and S. Xia, "Influence of armature movement velocity on the magnetic field distribution and current density distribution in railgun," *IEEE Transactions on Plasma Science*, Vol. 48, No. 6, 2308–2315, 2020.

[4] Li, S., J. Li, S. Xia, Q. Zhang, and P. Liu, "Phase division and critical point definition of electromagnetic railgun sliding contact state," *IEEE Transactions on Plasma Science*, Vol. 47, No. 5, 2399–2403, 2019.

[5] Sun, J., J. Cheng, Q. Wang, L. Xiong, Y. Cong, and Y. Wang, "Numerical simulation of melt-wave erosion in 2-D solid armature," *IEEE Transactions on Plasma Science*, Vol. 50, No. 4, 1032–1039, 2022.

[6] Stefani, F. and J. V. Parker, "Experiments to measure gouging threshold velocity for various metals against copper," *IEEE Transactions on Magnetics*, Vol. 35, No. 1, 312–316, 1999.

[7] Lu, J., X. Wu, S. Tan, Y. Zhang, and B. Li, "An initial survey of the life of rail for electromagnetic launch," *IEEE Transactions on Plasma Science*, Vol. 47, No. 5, 2228–2232, 2019.

[8] Sun, J., J. Cheng, Q. Wang, L. Xiong, Y. Cong, and Y. Wang, "Research on arc suppression parameter matching of augmented electromagnetic launcher," *IEEE Transactions on Plasma Science*, Vol. 49, No. 12, 3988–3993, 2021.

[9] Schneider, M., D. Eckenfels, and S. Nezirevic, "Doppler-radar: A possibility to monitor projectile dynamics in railguns," *IEEE Transactions on Magnetics*, Vol. 39, No. 1, 183–187, 2003.

[10] Meger, R. A., R. L. Cairns, S. R. Douglass, B. Huhman, J. M. Neri, C. J. Carney, H. N. Jones, K. Cooper, J. Feng, T. H. Brintlinger, *et al.*, "EM gun bore life experiments at naval research laboratory," *IEEE Transactions on Plasma Science*, Vol. 41, No. 5, 1533–1537, 2013.

[11] Motes, D., J. Keena, K. Womack, F. Stefani, and M. Crawford, "Thermal analysis of high-energy railgun tests," *IEEE Transactions on Plasma Science*, Vol. 40, No. 1, 124–130, 2012.

[12] Nie, J.-X., J.-J. Han, Q.-J. Jiao, Z.-X. Jin, and F. Zhang, "Effect of rail-type electromagnetic launcher dimensions on inductance

gradient," *High Voltage Engineering*, Vol. 36, No. 3, 728–732, 2010.

[13] Keshtkar, A., "Effect of rail dimension on current distribution and inductance gradient," *IEEE Transactions on Magnetics*, Vol. 41, No. 1, 383–386, 2005.

[14] Gong, F. and C. Weng, "3-D numerical study of meltwave erosion in solid armature railgun," *High Voltage Engineering*, Vol. 40, No. 07, 2245–2250, 2014.

[15] Shvetsov, G. A. and S. V. Stankevich, "Comparison between 2-D and 3-D electromagnetic modeling of railgun," *IEEE Transactions on Magnetics*, Vol. 45, No. 1, 453–457, 2009.

[16] Shvetsov, G. A. and S. V. Stankevich, "Three-dimensional numerical simulation of the joule heating of various shapes of armatures in railguns," *IEEE Transactions on Plasma Science*, Vol. 39, No. 1, 456–460, 2011.

[17] Hsieh, K., "A lagrangian formulation for mechanically, thermally coupled electromagnetic diffusive processes with moving conductors," *IEEE Transactions on Magnetics*, Vol. 31, No. 1, 604–609, 1995.

[18] Hsieh, K.-T., "Hybrid FE/BE implementation on electromechanical systems with moving conductors," *IEEE Transactions on Magnetics*, Vol. 43, No. 3, 1131–1133, 2007.

[19] Lin, Q. and B. Li, "Field-circuit coupled analysis of a series-augmented electromagnetic railgun," *IEEE Transactions on Plasma Science*, Vol. 48, No. 6, 2287–2293, 2020.

[20] Lin, Q. and B. Li, "Modeling and simulation of electromagnetic railgun launching process based on a transient multi-physical field solver," *Acta Armamentarii*, Vol. 41, No. 9, 1697–1707, 2020.

[21] Wang, G.-H., L. Xie, Y. He, S.-Y. Song, and J.-J. Gao, "Moving mesh FE/BE hybrid simulation of electromagnetic field evolution for railgun," *IEEE Transactions on Plasma Science*, Vol. 44, No. 8, 1424–1428, 2016.

[22] Satapathy, S. and K. Hsieh, "Jump conditions for Maxwell equations and their consequences," *AIP Advances*, Vol. 3, No. 1, 012120, 2013.